Feasibility studies of Ω^- baryon production at KLF and detector construction in the lab

Max Generowicz

April 26, 2024

<div style="border: 1px solid black; text-align: center;">

CONTENTS

</div>

Abstract

The KLF experiment at Jefferson Lab will — starting in 2026 — explore and measure particles containing strange quarks and probe the strong force. This project focusses on the simulation of the Ω^- hyperon events that will be observed within the GlueX detector. Jointly, this project will describe the testing and assembly of a plastic scintillator detector test station which will be used to test various KLF-related detectors and which is scheduled for use in the Crystal Ball experiment at MAMI.

Kinematics simulations of the KLF project yield results which predict that in the 100 day runtime of the experiment, around 6000 fully reconstructible events involving the Ω^- should be observed.

The plastic scintillator (Eljen EJ-204) and wrapping (Mylar) configuration used in the detector test station is measured to have an apparent attenuation length of $\lambda = (7 \pm 1)$ cm due to imperfect light retention.

CHAPTER

1

INTRODUCTION

1.1   Elementary particles and quarks

In the Standard Model of physics, our current most complete theory of particle physics, everything is reduced to 17 elementary particles[1]. These particles are grouped into *fermions* (the main constituents of matter) and *bosons* (particles which carry the fundamental forces of nature). Fermions in turn are separated into *quarks* — which carry a colour charge and thus interact via the strong interaction — and *leptons* — which do not.

The quarks themselves, which make up the majority of the matter surrounding us, come in 6 different "flavours": up (u), down (d), charm (c), strange (s), top (t) and bottom (b). These can then be grouped into three generations of quarks (which nicely match the three generations of leptons), with each generation containing an up-type quark of electric charge $+\frac{2}{3}$ and a down-type quark of electric charge $-\frac{1}{3}$. These generations are, in ascending mass order, up and down (generation 1), charm and strange (generation 2) and top and bottom (generation 3).

Essentially all of the matter on Earth which we interact with on a daily basis is made of just the first-generation quarks: up and down. These are combined into composite particles called *hadrons*, with special names given to particles formed of two (*mesons*) and three (*baryons*) quarks. The most abundant and stable examples of baryons are protons and neutrons, which constitute the vast majority of visible matter surrounding us.

Quarks interact via the weak and electromagnetic interactions but also via the strong interaction, a property which makes them unique among all the particle families. Furthermore, the study of quarks — and by extension the study of the strong interaction — can shed light on the properties and behaviour of the gluon (g), the boson responsible for mediating the strong force.
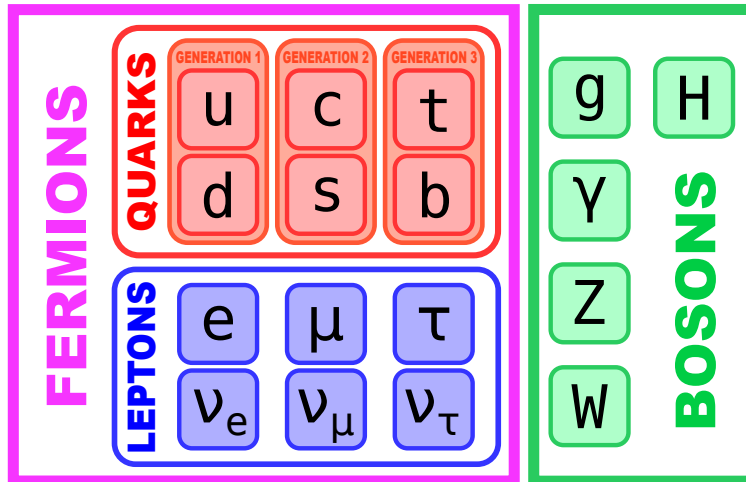
Figure 1.1: Classic Standard Model table with the division into bosons and fermions shown. The separation of fermions into leptons and quarks is also shown, as well as the subsequent grouping of the quarks into generations.

1.2   Hyperons and Ω^-

Hyperons are simply baryons with at least one strange quark and no other heavier quarks (i.e. no charm or bottom quarks). However, hadrons made of quarks other than the first generation quarks are only really seen on Earth in labs and accelerators. This is for a simple reason: the higher the generation of quark, the heavier it is. Therefore, the processes required to produce them involve energies on a scale larger than commonly observed in nature (on Earth). Furthermore, the heavier quarks quickly decay into the lighter flavours, so any matter made of the later generations of quarks will tend to have very short lifetimes.

Because of this, the prime locations for finding strange matter[1] are inside high-energy accelerators and neutron stars. Neutron stars are collapsed cores of giant stars, which makes them very dense objects. This density causes huge pressures which would compress the matter inside them and create conditions which would be favourable to strange quark creation[2]. Thus, hyperons are very rarely observed on Earth (and only in very particular environments) but could well form naturally in neutron stars[3].

Aside from the astronomical interest of neutron stars, the second and third generation quarks are still relatively unknown, so any experiment probing their properties is of interest to the field. Furthermore, some properties of these quarks that are measured can be used as parameters to theoretical models such as QCD (quantum chromodynamics). Strange quarks are of particular interest as they are the lightest of the second and third generation quarks, so are the easiest quarks beyond the first generation to produce and are the obvious first step to the exploration of heavier quarks.

Therefore, a very interesting hyperon to consider is the Ω^- particle, which is the strangest possible baryon as it is composed of three strange quarks: *sss*.

---

[1]Matter made of strange quarks

1.3 Jefferson Lab, GlueX and KLF

The Thomas Jefferson National Accelerator Facility, or JLab for short, is a particle accelerator facility in Virginia, US. The facility is comprised of a beamline which accelerates electrons up to 12 GeV and four halls to which the electrons can be diverted, in which different experiments are housed.

Hall D at Jefferson Lab houses the GlueX detector. This detector is (roughly) cylindrical in shape, complete with a time-of-flight system, calorimeter and solenoid (Figure 2.1). These features allow the detection and discrimination of various particles which in turn allows precise reconstruction of any particle decay processes occurring within the detector.

The K-Long facility (KLF), tightly linked to the KLF project, is an experiment which plans to discover, quantify and otherwise measure the particles and interactions associated with strange quarks. This would have impacts not only in hadron physics (for the reasons mentioned previously) but also in cosmology and astrophysics, through the link to neutron stars and the cooling of the early universe.

The KLF project plans, starting in 2026, to use the existing electron beamline to generate a beam of kaons[2] which will be fired upon a liquid hydrogen (and subsequently deuterium) target[4]. The decay products of the resulting interactions (an assortment of hyperons as well as other more "ordinary" particles) will be detected by the existing GlueX detector. However, as this planned kaon beam will carry a flux many[3] times larger than previous kaon experiments and given all the other unknowns in the experiment, an important part of the pre-experimental phase is studying the expected number of events observed during the runtime of the experiment. One of the main goals of this particular project will be to focus on the Ω^- events.

1.4 Detector construction

While some projects have the luxury of using pre-existing detectors, these detectors need to be built at some stage. Furthermore, as different experiments investigate different facets of particle physics, they will all need detectors with slightly different strengths and specifications. Occasionally, changing detector designs will lead to discoveries which represent paradigm shifts in detector construction. For example, the invention of the time projection chamber was revolutionary in that it allowed the 3D reconstruction of particle trajectories, and it is now a common feature of many particle physics detectors.

Judging the performance of a particular detector is also a very important in determining its feasibility for certain applications. To do this, one can analyse the results obtained from said detector or use a different detector as a diagnostic tool for the original detector. The second main goal of this project is to construct such a detector test station, first to test various detectors to be used in the scope of the KLF project, and then with its final destination being the Crystal Ball detector[5].

---

[2]Specifically long-lived neutral kaons K_L^0, also called K-Long, hence the name of the project.
[3]About 1000

CHAPTER

2

METHODOLOGY

2.1   KLF experiment

In the following sections, an outline of the existing KLF experiment infrastructure will be given.

2.1.1   Current GlueX beamline

The KLF project will use the existing GlueX beamline to generate the kaons necessary for the experiment. The GlueX beamline itself uses the main CEBAF[1] electron beam to generate a photon beam.

The CEBAF electron beam finished an upgrade in 2017 to increase its energy from 6 to 12 GeV[6]. A diamond radiator is then used as the electron beam approaches Hall D to create a linearly-polarized photon beam, by orienting the diamond radiator in a specific way[7]. Any surviving electrons are diverted into an electron dump using a magnetic field, but the photons are focussed using a collimator 75m downstream of the diamond radiator. This ensures a narrow photon beam that can be precisely aimed at a target within the detector[2].
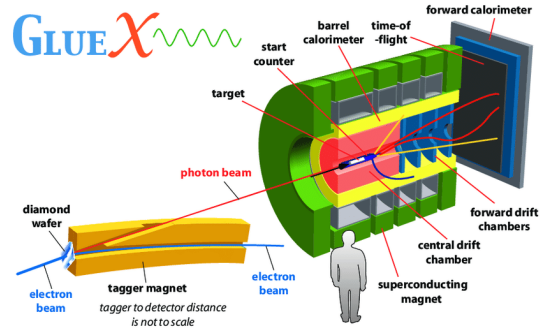
A small gap in the detector is left for the remaining photons to traverse, so they can safely deposit their energy in a photon dump placed behind the GlueX detector.

---

[1]Continuous Electron Beam Accelerator Facility

[2]Note: this electron to photon beam concept and technology is named Compact Photon Source (CPS) and currently being developed and tested by the CPS collaboration.
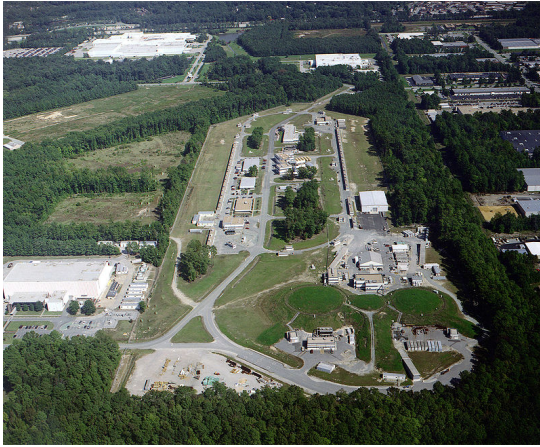
(a) Jefferson Lab, Newport News, Virginia, US.   (b) Diagram of the GlueX detector and photon beam.

Figure 2.1: Aerial view of Jefferson Lab (left) and a schematic cut view of the GlueX detector (right). Note: the image of JLab (Figure 2.1a) was taken in 2010, before the construction of Hall D.

2.1.2 Kaon beam

Using the established photon beam, the KLF project plans to generate a kaon beam. To do this, a beryllium target (referred to as the Kaon Production Target or KPT) is placed downstream of the CPS. This induces the photoproduction of the $\phi[s\bar{s}]$ meson through the reaction $\gamma p \rightarrow p\phi$. The ϕ meson then decays into both short and long-lived neutral kaons ($\phi \rightarrow K_L^0 + K_S^0$). However, as the KPT is placed 24m upstream of the target within the detector, all of the short-lived kaons decay by the time the beam reaches the target and so we can consider the beam to be a pure long-lived kaon beam (usually referred to as the K_L beam). This is shown in the diagram in Figure 2.2.
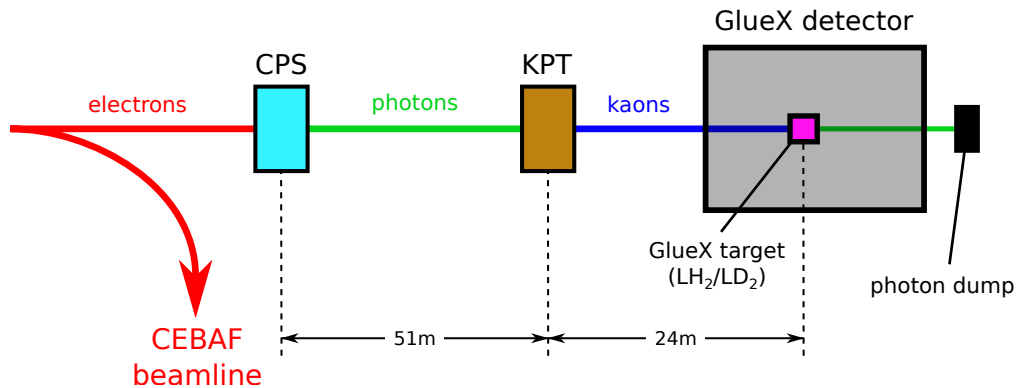
Figure 2.2: Simplified diagram of the Hall D beamline. The CEBAF electron beam is converted to a photon beam, which in turn is converted into a K_L beam. This final beam is incident on the liquid hydrogen/deuterium target in the GlueX detector. Any remaining photons are deposited in the photon dump.

Extensive simulations have already been carried out in order to determine the optimal parameters for the production of the kaon beam, including the material of the KPT, the distance from the KPT to the detector target, and many others[8]. Slight changes have also been proposed to the current

GlueX setup such as increasing the size of the liquid hydrogen/deuterium target cell[3], again to maximize the possible physics of the new KLF experiment.

2.2 Ω^- production simulations

To assess the viability and the expected outcome of the physics observed in the new data-taking runs, simulations are performed. The following sections outline the theory and implementation of these simuations.

2.2.1 Ω^- production in GlueX

The Ω^- baryon, which is the focus of this particular dissertation, is obtained through the collision of the kaon beam with the protons in the liquid hydrogen target, through the interaction $K_L^0 + p \rightarrow K^+ + K^+ + \Omega^-$. However, the Ω^- will decay[4] into a K^- and a Λ hyperon (which is also of interest to the KLF project, but not the subject of this study). The Λ baryon further decays into a negative pion and a proton. This chain of decays is depicted in Figure 2.3.
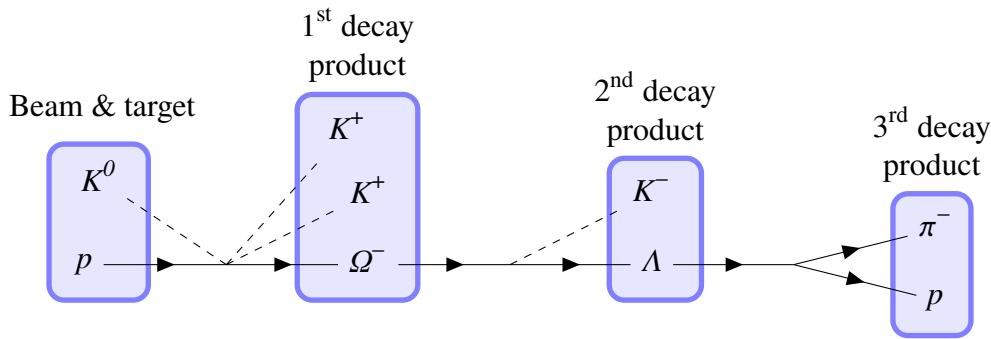

Figure 2.3: Chain of interactions produced inside GlueX which contain the Ω^- baryon of interest.

Very rarely will the Ω^- itself be detected[5]. Instead, it is these non-hyperon decay products that can be detected (and relatively easily identified, as they are charged) by the GlueX detector and are crucial to the reconstruction of the Ω^- event as they carry polarization and energy information relating to it. While the two positive kaons must be detected for any reconstruction to be possible, one of the remaining non-hyperon decay products can remain undetected with a reconstruction still being possible[6]. This leads to 6 separate so-called *detection cases*[7], some of which allow a full reconstruction of the event, some which allow a partial reconstruction with polarization information for the Λ particle, and one which allows reconstruction of the Ω^- particle only. These cases are detailed in Table 2.1.

---

[3]From a cylinder of 2cm diameter and 30cm length to a cylinder of 6cm diameter and 40cm length.

[4]The mean lifetime of Ω^- is $8.21 \cdot 10^{-11}$ s[9].

[5]As it will decay before reaching the sensitive regions of the detector.

[6]The pion and proton can both be omitted, as they can be thought of as the single Λ particle.

[7]In the code and subsequent graphs, these detection cases are named by the missing particles (to reduce name length). Thus we have the cases: "Missing none", "Missing K^-", "Missing p, π^-", "Missing K^-, p, π^-", "Missing π^-" and "Missing p".

Detected particles	Undetected particle(s)	Type of reconstruction
K^+, K^+, K^-, p, π^-	none	full
K^+, K^+, p, π^-	K^-	full
K^+, K^+, K^-	p, π^-	full
K^+, K^+	K^-, p, π^-	Ω^-
K^+, K^+, K^-, p	π^-	Λ polarization
K^+, K^+, K^-, π^-	p	Λ polarization

Table 2.1: Table of cases in which reconstruction of the event is possible. The left column shows the particles that are detected and the centre column shows the particles that have escaped detection in that particular scenario. The right column shows which reconstruction is possible with the given detected particles.

It is important to note that these categories are not exclusive: that is to say that a particular event can correspond to more than one detection case. For example, detecting two positive kaons, a negative kaon and a proton will be classified under all three of "Missing p, π^-", "Missing K^-, p, π^-" and "Missing π^-".

2.2.2 ROOT kinematic simulations

The first step in studying the expected outcome of the experiment is to perform simple kinematics simulations of the particles produced in the GlueX detector. This will determine which (and how many) events will be observable by the detector given the characteristics of said detector, which in turn determines the scope of physics possible.

Simulation details

To perform these simulations, the ROOT[10] software is used. ROOT is a framework developed by CERN, written mostly in C++, which focusses on data analysis for high energy physics and treating large amounts of data. A basic ROOT simulation was written to simulate the decay chain containing the Ω^- (shown in Figure 2.3), incorporating the kaon beam energy distribution (Figure 2.4a). The heart of the code is ROOT's `TGenPhaseSpace` class, which is used to generate the phasespace weights of the different decay products — which can essentially be viewed as the probability of a particular energy distribution among the particles — for each decay. This class is built upon an older Fortran function (GENBOD[8], function W515 from CERNLIB), which uses the Raubold and Lynch method[11].

---

[8]https://cernlib.web.cern.ch/mc/genbod.html

Angular dependence

It is then possible to generate 2-dimensional histograms showing the most likely angles and momenta at which each particle will be found after the interactions. These histograms (called *angular dependence histograms*) must take into account the energy cutoff of the detector (anything under 300 MeV cannot be reliably detected) as well as the non-total hermeticity of the GlueX detector: only particles in the angle[9] ranges $1° \leq \theta \leq 11°$ and $29° \leq \theta \leq 132°$ can be detected[7]. An example of such a histogram is shown in Figure 2.4b.

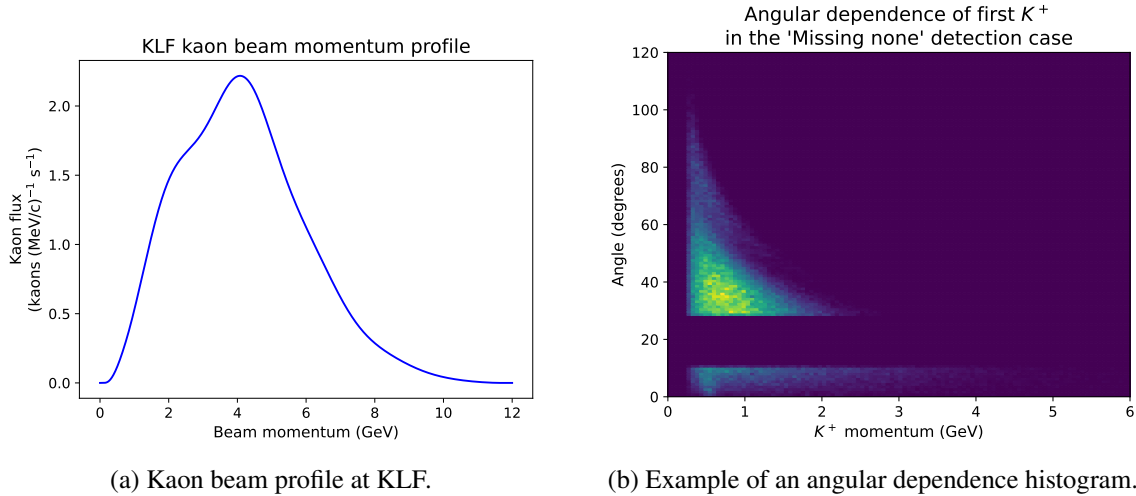(a) Kaon beam profile at KLF.   (b) Example of an angular dependence histogram.

Figure 2.4: Beam profile of the KLF kaon beam incident on the GlueX target (left). On the right, an example of an angular dependence histogram generated by the ROOT kinematics simulation. In this particular case, the graph corresponds to the one of the K^+ generated in the first decay, in the detection case where all particles are detected.

Beam acceptance

The next step is to generate histograms which show the proportion of events which result in all the relevant particles being detected depending on the momentum of the incoming kaon — this for all six detection cases. These are called *beam acceptance histograms*, and are simply obtained by dividing the histogram of the amount of events satisfying the detection case (notated C for "case counts") by the histogram of the total number of kaons used to generate these events (notated B for "beam counts")[10]. In other words, the beam acceptance is $\frac{C}{B}$.

In reality, the beam acceptance must be a smooth function, so a fourth order polynomial is fit to the histogram and is used as the beam acceptance for subsequent calculations. The error on the beam acceptance is taken to be the error on the fit of the polynomial to the simulation data.

---

[9]This angle is the polar angle in the physics convention, assuming the beam points in the z direction. In other words, it is the angle away from the beamline.

[10]These are both histograms as they depend on beam momentum.

Total number of events

It is now possible to calculate the total number of events that are predicted to be observed during the 100 day runtime of the experiment, for each detection case. To do this the formula for luminosity is used[12], in addition to the fact that the molar density is given by $\rho_T = \frac{N_A}{M_H}\rho$ (where N_A is Avogadro's number, M_H the molar mass of the target element: hydrogen, and ρ the density of the target) and that each detection case has an acceptance which must be multiplied on. This yields the following equation for the total number of events observed over a time t (in seconds) for a particular detection case c, per MeV[11]:

$$N_c(p_K) = \Phi(p_K) \cdot \frac{N_A}{M_H}\rho \cdot l \cdot A_c(p_K) \cdot \sigma(p_K) \cdot t \qquad (2.1)$$

where Φ is the kaon beam flux, l is the target length, A is the beam acceptance and σ is the Ω^- production cross-section from the kaon-hydrogen target interaction. Furthermore, the values with beam momentum dependence have been indicated with (p_K).

Using equation (2.1) generates a histogram of total number of events expected per MeV. To obtain an absolute total number of events, these events are simply added up over all energies.

---

[11]Indeed, this N has units of MeV^{-1}. This may seem strange at first, but it is due to the fact that the kaon beam flux is expressed in kaons $\text{s}^{-1}\,\text{MeV}^{-1}$. Intuitively, it is beneficial to think of the total number of events N as a histogram with bins of 1 MeV wide.

2.3 Detector test station construction

The next sections present the concept, assembly and testing procedures of the diagnostic detector.

2.3.1 Detector concept

As mentioned briefly in the introduction, the aim of this part of the project is to construct a scintillation detector which other detectors can be placed inside, thus allowing it to be used to calibrate, diagnose and test the inner detector. Furthermore, the geometry of the detector in which it will be placed restricts the size and shape of certain components. These factors mean that the final detector will be composed of 24 separate plastic Eljen EJ-204 scintillators[13], arranged in a cylinder so as to surround the inner detector. Furthermore, to ensure full hermeticity, each the shape of the scintillators has been carefully designed (see Appendix A) so that one edge is slightly angled: this allows the scintillators to form the cylindrical barrel without leaving any gaps, as shown in Figure 2.5a.

The scintillators are covered in Mylar to trap and reflect the scintillation light. The energy resolution of the detector increases the more scintillation light can be trapped within the scintillator. While Mylar is quite reflective (around 95%), total internal reflection is much more effective for reflection (essentially 100%) and the range of angles for which total internal reflection is allowed increase as the difference between the refractive indices of the two media increases. For this reason, the Mylar is crumpled to leave air gaps between the scintillator and Mylar, as the difference between the refractive indices of air and the scintillator is larger than between that of Mylar and the scintillator. The scintillators are further wrapped in Tedlar and the whole barrel is wrapped in a black cloth (both of these to prevent light leakage into the scintillator).

The scintillation light is detected by a silicon photomultiplier[12] (SiPM) pressed against the face of the scintillator and is used to determine the energy of the particle deposited in the scintillator. Connecting the SiPMs from scintillators on opposite sides of the barrel to the same multichannel analyzer (MCA) will allow for meaningful timing data to be collected as well. This, combined with the spatial segmentation provided by the separate scintillators will allow the rough reconstruction of the path and direction of particles passing through the detector.

### 2.3.2 Scintillator testing and characterization

In order to obtain meaningful information from the scintillators, their response to energy deposited in them at different positions must be measured. To do this, a simple test setup is used: a single scintillator is wrapped in Mylar, Tedlar and black cloth[13]. The SiPM is pressed against the face of the scintillator — using silicone optical grease as the interface between the scintillator and the SiPM — and connected as per the example on the Hamamatsu data sheet for the MPPC module[14]. This involves connecting the MPPC module board to a bias supply of ±5 V ("typical" value according

---

[12]The specific module used for this detector is Hamamatsu's MPPC C13367 series[14].

[13]This mimics the layers present in the final detector, although the Tedlar will be wrapped around groups of 6 scintillators collectively instead of each scintillator individually. The black cloth recreates the dark conditions inside the Crystal Ball.

(a) Render of the final scintillator configuration.
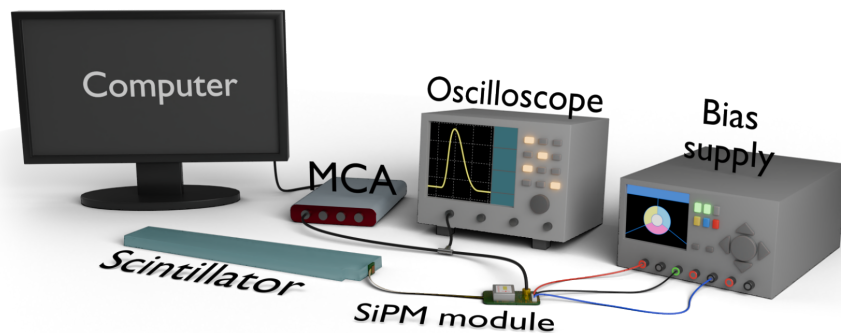
(b) Scintillator testing setup.

Figure 2.5: Top: 3D render of the Mylar-wrapped scintillators, arranged in the final cylindrical form of the detector. These will be held in place by a 3D printed support structure (see Appendix A). Bottom: diagram of the experimental setup used to test the plastic scintillator (note that during data taking, the scintillator would be wrapped in Mylar, Tedlar and black cloth).

to Hamamatsu) and connecting the output of the board to an oscilloscope and the multichannel analyzer (MCA). The MCA is then connected to a computer for data recording and storage. This setup is shown in the diagram in Figure 2.5b. When light is detected by the SiPM, it will generate a pulse (which, incidentally, is visible on the oscilloscope as the SiPM turns photons into voltage). The computer software will store the height of these pulse peaks, corresponding to the amount of photons detected. This can then be plotted as a spectrum of signal peak heights, which are a proxy for energy (as the number of photons generated by the scintillation are themselves a proxy for energy deposited in the scintillator).

A collimated ^{90}Sr (185kBq) source is used to test the response of the scintillator. This is an electron source so — contrary to using γ sources — there will be no Compton edge in the final spectrum, which would usually serve as a reference point to compare different measurements. Therefore, in order to make comparable measurements, the data must be taken for the same amount of time in each measurement (as this ensures the same amount of electrons incident on the scintillator). However, a benefit of using a collimated source is that the location of the interactions in the scintillator can

be precisely controlled, which allows the light falloff (or *apparent attenuation length*[14]) inside the scintillator to be determined. To do this, measurements are performed with the source at different locations along the scintillator's length and breadth (Figure 2.6a). The spectra recorded from these measurements (Figure 2.6b) can then be fit with the inverted sigmoid

$$\sigma(x) = \frac{L}{1 + e^{k(x-x_0)}} \tag{2.2}$$

which provides a consistent analytic form across all measurements. The centre of the sigmoids x_0 is then used as a proxy for the "amount of light" which reaches the SiPM. Plotting this amount of light as a function of the distance of the source away from the SiPM, the exponential

$$N(x) = Ae^{-\frac{x-x_0}{\lambda}} + y_0 \tag{2.3}$$

is fit to the plot to yield the apparent attenuation length λ.

(a) Approximate ^{90}Sr source positions for measurements.

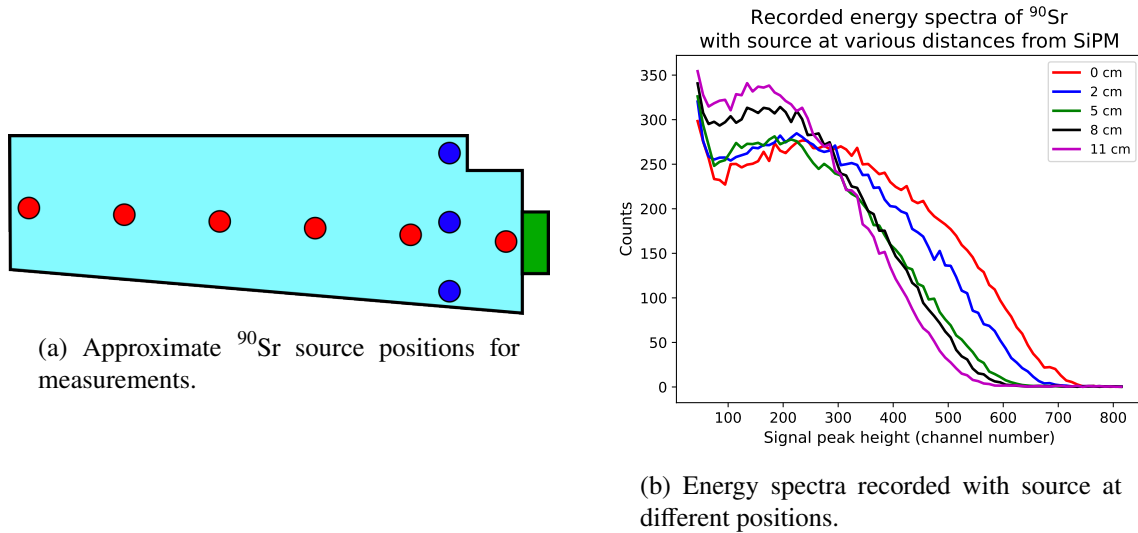(b) Energy spectra recorded with source at different positions.

Figure 2.6: Approximate location of the ^{90}Sr source for the different measurements for light falloff inside the scintillator (left). The red measurements vary the distance to the SiPM whereas the blue measurements vary the lateral position of the source. Note that the diagram is not to scale and the size of the notch in particular has been exaggerated. On the right, an example of a few measurements made of the energy spectrum of ^{90}Sr with the source at different distances away from the SiPM. Note that the "signal peak height" can be read as energy with arbitrary units.

2.3.3 Detector assembly and further testing

After testing of a single scintillator, all of the scintillators can be assembled into the final detector. To do this, a 3D printed support structure is used. This support structure contains slots for all of the

---

[14]It is an "apparent" length because it is not truly due to the attenuation of light by the scintillator material. Instead, it is caused by the loss of light due to the non-perfect reflectivity of the Mylar.

24 scintillators, as well as threaded holes to screw the SiPM module boards in place and cushioned screw elements to press the SiPMs against the scintillator face.

The assembly of the detector is simple as the scintillators slide easily into their designated slots. A small part of the Mylar wrapping on the SiPM face of the scintillator is cut away to make space for the SiPM and optical silicone grease is used as the medium between the SiPM and the scintillator.

Once the SiPMs, SiPM boards and scintillators have been fixed in place using the various screws and rods designed for that purpose, the scintillators can be wrapped in Tedlar (in groups of 6, i.e. by quarters of the barrel) and the whole detector surrounded by blackout material[15]. Then, each SiPM board is connected to the bias supply and tested in the same way as described above for the single scintillators.

---

[15]Multiple layers of bin bag as well as black cloth were used in this particular case.

CHAPTER

3

RESULTS

## 3.1 Ω^- simulations

Once the simulations have been run, different results can be extracted as mentioned above.

3.1.1 Beam acceptance

The beam acceptance histograms can be generated using the process described above, including their errors calculated by the fit. These are compiled in Figure 3.1a.

These acceptance histograms all show a prominent feature: the acceptance is zero up to about 3 GeV. This is due to the minimum energy required to create the Ω^- hyperon. This threshold momentum for the kaon beam can be theoretically calculated to be at 3.13 GeV, but it also arises naturally through simulation. These plots also show — rather intuitively — that the more restrictive detection cases (i.e. those which require more particles to be detected, for example "Missing none") are less likely to happen than the less restrictive cases (e.g. "Missing K^-, p, π^-").

Additionally, these beam acceptances can be used to obtain an "average acceptance" for each detection case (shown in Table 3.1b). This is done by multiplying the kaon beam profile (shown in Figure 2.4a) by the acceptance curve and taking the average. In other words, this average acceptance in the average beam acceptance, weighted with the kaon flux. This is a particularly useful result as it gives a more realistic idea of the acceptance of each case (given that a lot more kaons carry 4 GeV than 12 GeV of energy), as well as combining two elements of the final equation (2.1): the beam acceptance $A_c(p_K)$ and the kaon flux $\Phi(p_K)$.
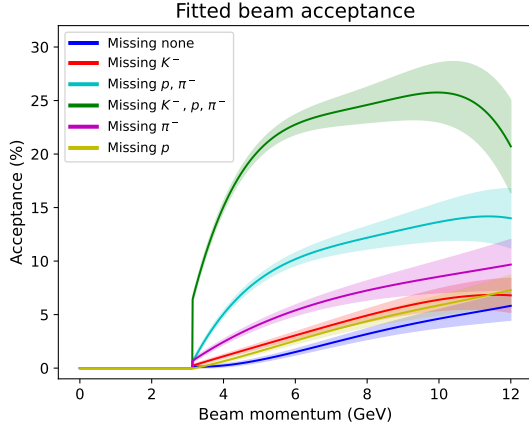
(a) Beam acceptance fitted with 4th degree polynomials.

Detection case	Average acceptance (%)
Missing none	0.7
Missing K^-	1.5
Missing p, π^-	5.1
Missing K^-, p, π^-	12.7
Missing π^-	2.7
Missing p	1.1

(b) Average beam acceptances, weighted with the kaon flux.

Figure 3.1: Fitted beam acceptance histograms with errors (left). Note that the scale has been modified to show the acceptance in percent. The $Ω⁻$ production threshold energy can also be seen at around 3 GeV. On the right, the average acceptance for each detection case, using the kaon beam profile as weighting.

3.1.2   Total number of events

These acceptances can now be used in equation (2.1) to determine the final number of events observed during the runtime of the experiment. The literature values of $N_A = 6.022 \cdot 10^{23} \, \text{mol}^{-1}$[15], $M_H = 2.016 \cdot 10^{-3} \, \text{kg mol}^{-1}$[16] are used — along with the KLF experiment-specific values of $\rho = (71.2 \pm 0.3) \, \text{kg m}^{-3}$, $l = 0.4 \text{m}$[7] and $t = 8640000 \, \text{s}$ (100 day runtime) — to compute the constant, or non-beam momentum dependent, part of equation (2.1):

$$C = (7.35 \pm 0.03) \cdot 10^{34} \, \text{s m}^{-2} \tag{3.1}$$

Now the beam dependent terms, which are the kaon flux, the $Ω⁻$ production cross-section and the acceptance, can all be multiplied together and by the constant C to yield the total number of events observed. Inputting the acceptance for each case will give us such a number for each case (which can then easily be converted into a number for each reconstruction case), all of which can be seen in Table 3.1.

These tables show that the overall total number of $Ω⁻$ events expected to be seen is slightly under 20000. Of these events, about half will allow reconstruction of the $Ω⁻$ particle only, about third will allow reconstruction of the $Λ$ polarization and about a fifth will allow full reconstruction of the event.

In general, these results are consistent with the average beam acceptances from Table 3.1b, in terms of the ratio of events in each detection case. This supports the validity of the concept of the average beam acceptance as more than just an helpful intuitive way of looking at the acceptance.

To put these numbers into context, the rule of thumb for experiments of this type is that one event per day is the cutoff point for a reasonable event rate. Using that benchmark, these results indicate

Detection case	Total number of events ($\cdot 10^3$)
Missing none	0.7 ± 0.1
Missing K^-	1.3 ± 0.2
Missing p, π^-	4 ± 0.3
Missing K^-, p, π^-	9.1 ± 0.4
Missing π^-	2.2 ± 0.2
Missing p	1.1 ± 0.1

(a) Total number of events, per detection case.

Reconstruction	Total number of events ($\cdot 10^3$)
Full	6 ± 0.6
Ω^-	9.1 ± 0.4
Λ polarization	3.3 ± 0.3

(b) Total number of events, per reconstruction.

Table 3.1: Tables showing the total number of relevant events predicted to be observed during the 100 day runtime of the KLF experiment. These are broken down by detection case (left) and by reconstruction possible from the observed decay products (right).

a predicted event rate which is well suited to the characterization of the Ω^- baryon, at around 10 to 100 events per day for each reconstruction case.

3.2 Detector test station

The section describes the results of the testing and characterisation of the scintillators as well as the assembly of the final detector.

3.2.1 Scintillator characterisation

As described in the method, a spectrum is recorded with the SiPM while holding the strontium 90 source at different distances from the SiPM end of the scintillator. This corresponds to the red measurements in Figure 2.6a. The spectra (similar to those shown in Figure 2.6b) are then fit with the sigmoid function described in equation (2.2) and their centres, given by the x_0 parameter, are then plotted on a graph. This graph is shown in Figure 3.2. The y axis can be thought of as a proxy for the number of photons detected by the SiPM, with the centre of the sigmoid being used to meaningfully compare the different spectra[1].
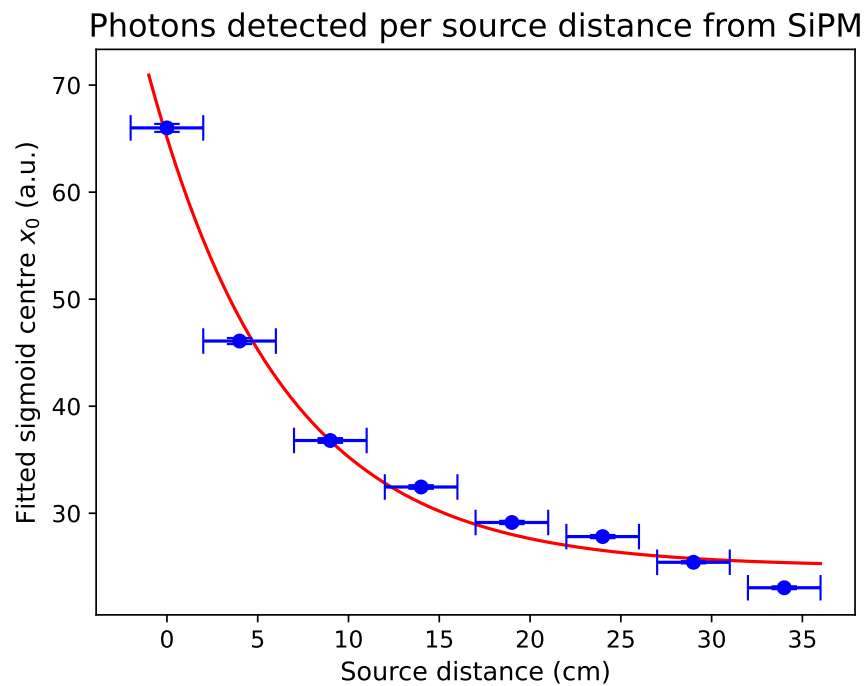

Figure 3.2: Plot of the amount of photons detected by the SiPM (represented by the centre of the sigmoid fitted to the spectrum) depending on the distance of the strontium source from the SiPM end of the scintillator. "a.u." denotes arbitrary units.

The error on x_0 is simply extracted from the covariance matrix of the fit returned by the fitting function[2]. The error on the distance is estimated as being ±2 cm, given the size of the strontium source and the difficulty in measuring distances from the cylindrical source to the SiPM, especially through many layers of wrapping.

---

[1]One could use different points of the sigmoid as the recorded value — for instance when the curve dips below a predefined threshold — or even different fit curves. However, the centre of the sigmoid is a fairly simple and consistent choice.

[2]Python's `scipy.optimize.curve_fit`.

Fitting an exponential to the data in Figure 3.2 yields the apparent attenuation length of the scintillator, given by the λ factor in equation (2.3), with the error obtained by the covariance matrix of the fit:

$$\lambda = (7 \pm 1)\,\text{cm} \tag{3.2}$$

This is a highly important result to keep in mind when using these scintillator going forwards: as the scintillators themselves are around 35cm long, the fact that the attenuation length is about a fifth of the full length of the scintillator will have a major impact on the ability of the detector to make precise energy measurements of particles[3]. For instance, two particles depositing identical amounts of energy on opposite ends of the scintillator will be detected as two vastly different amounts of photons by the SiPM.

However, it is also crucial to remember that this is not the true attenuation length of the scintillator[4], which is to say that it is not an intrinsic property of the scintillator. Rather, it reflects the absorption properties of the wrapping material and its ability to keep light contained in the scintillator until it reaches the SiPM[5].

The measurements shown in blue in Figure 2.6a were also performed, in order to determine the variation in detection of particles depositing their energy in various lateral positions of the scintillator (specifically, the effect of the notch on the amount of detected photons is of interest). However, the differences between these lateral measurements are comparable to the errors associated with these measurements, so it can be considered that the lateral position of the source has no effect on the amount of photons detected.

3.2.2 Detector assembly

The detector is now assembled as described in the previous chapter. Some imperfections can arise in the support structure due to small 3D printing defects, the most important being the size of the scintillator slots — in particular if the slots are to small to fit the scintillator ends. This can easily be rectified by filing away some of the filament material to make the slots large enough.

The SiPMs are connected and verified to yield the expected characteristic pulse shape. For this testing process, no radioactive sources are needed as the precise energy of the incident particles is not important. Instead, background cosmic radiation are sufficient to show that the setup does indeed produce a relevant signal.

---

[3]As a reminder, the attenuation length λ is the distance by which 63% of the particles have been stopped.

[4]Indeed, this is in reality 160cm[13].

[5]Of course, this apparent result is a combination of the true attenuation length and the reflectivity of the wrapping. However, given the order of magnitude difference between the two, the reflectivity component of this apparent attenuation length dominates and the true attenuation length of the scintillator can essentially be ignored.

CHAPTER

4

CONCLUSIONS

4.1 KLF simulations

The kinematics simulations were successfully used to obtain a prediction about the number of events observed during the runtime of the experiment, with around 6000 expected fully reconstructible events in 100 days. As mentioned in the previous chapter, this corresponds to a daily rate of about 60 events, which is an order of magnitude higher than the generally accepted feasible minimum of one daily event of interest. This suggests that the statistics gathered should be sufficient to gather significantly newer and more data about the Ω^- particle than any previous experiment.

Another use of these kinematic simulations, not explored in depth in this document, is the angular dependence of each particle. An example of this can be seen in Figure 2.4b and will further help determine the expected signal from these events, given that different parts of the GlueX detector have different detection properties and capabilities.

The next step in the preparation in the lead up to the start of the runs in 2026 will be to perform more complex 3D simulations using a combination of ROOT and GEANT4[17]. These will allow an even more accurate depiction of the expected signals from the detector, which in turn will give a far more realistic idea of the physics possible in the scope of the KLF experiment.

4.2 Detector test station construction

The plastic scintillators used in the detector test station were tested, finding an apparent attenuation length of 7cm. This is a significant result as this attenuation length is far smaller than the length of the scintillators themselves, which will impact the significance and analysis of measurements taken

with them. However, as mentioned in the previous chapter, this attenuation length can be improved by increasing the light retention of the scintillator-wrapping system. This could be achieved by changing the wrapping method or material.

The wrapped plastic scintillators were also successfully installed on the support structure, with a signal being obtained from the assembled detector. This detector test station can now be used for different applications, the main one of which will be to test different detector components for the KLF project. One benefit of this detector test station is that the only restriction imposed on its design is the geometry of the Crystal Ball detector (which is our detector's final planned[1] destination). This means that it is particularly versatile and should be suited to a range of different uses.

---

[1]As of April 2024.

BIBLIOGRAPHY

[1] Mann RB. An introduction to particle physics and the standard model. Boca Raton, FL: CRC Press; 2010.

[2] Klähn T, Blaschke DB. Strange matter in compact stars. EPJ Web of Conferences. 2018;171:08001. Available from: http://dx.doi.org/10.1051/epjconf/201817108001.

[3] Schaffner-Bielich J, Hanauske M, Stöcker H, Greiner W. Phase Transition to Hyperon Matter in Neutron Stars. Physical Review Letters. 2002 Oct;89(17). Available from: http://dx.doi.org/10.1103/PhysRevLett.89.171101.

[4] Dobbs S. Strange Hadron Spectroscopy with the KLong Facility at Jefferson Lab; 2022.

[5] Collaboration A. Crystal Ball; 2018. Available from: https://wwwa2.kph.uni-mainz.de/a2detector-system/crystal-ball/.

[6] JLab. 12 GeV Upgrade; 2023. Available from: https://www.jlab.org/physics/GeV.

[7] Adhikari S, Akondi CS, Al Ghoul H, Ali A, Amaryan M, Anassontzis EG, et al. The GlueX beamline and detector. Nuclear Instruments and Methods in Physics Research Section A: Accelerators, Spectrometers, Detectors and Associated Equipment. 2021 Jan;987:164807. Available from: http://dx.doi.org/10.1016/j.nima.2020.164807.

[8] Collaboration K, Amaryan M, Bashkanov M, Dobbs S, Ritman J, Stevens J, et al.. Strange Hadron Spectroscopy with Secondary KL Beam in Hall D; 2021.

[9] Workman RL, Others. Review of Particle Physics. PTEP. 2022;2022:083C01.

[10] Brun R, Rademakers F. ROOT - An Object Oriented Data Analysis Framework. In: AIHENP'96 Workshop, Lausane. vol. 389; 1996. p. 81-6.

[11] James F. Monte-Carlo phase space. CERN-68-15. 1968 5.

[12] Concept of luminosity;. Available from: https://cds.cern.ch/record/941318/files/p361.pdf.

[13] General Purpose Plastic Scintillator EJ-200, EJ-204, EJ-208, EJ-212;. Available from: https://eljentechnology.com/images/products/data_sheets/EJ-200_EJ-204_EJ-208_EJ-212.pdf.

[14] MPPC modules, C13367 series;. Available from: https://www.hamamatsu.com/content/dam/hamamatsu-photonics/sites/documents/99_SALES_LIBRARY/ssd/c13367_series_kacc1269e.pdf.

[15] BIPM. Le Système international d'unités / The International System of Units ('The SI Brochure'). Ninth ed. Bureau international des poids et mesures; 2019. Available from: http://www.bipm.org/en/si/si_brochure/.

[16] Kim S, Chen J, Cheng T, Gindulyte A, He J, He S, et al. PubChem 2023 update. Nucleic Acids Research. 2022 10;51(D1):D1373-80. Available from: https://doi.org/10.1093/nar/gkac956.

[17] Agostinelli S, et al. GEANT4–a simulation toolkit. Nucl Instrum Meth A. 2003;506:250-303.

Appendix A

Detector design details

The following is a compilation of techniques, templates, models and general information about the design of the detector test station and the process followed to assemble it.

A.1   Plastic scintillators

The scintillators used are Eljen EJ-204[13]. Their shape has been specially designed (Figure A.1) to provide hermetic coverage when assembled in a barrel shape, all while adhering to the restrictions imposed by the location in which the detector will be used (within the Crystal Ball detector).
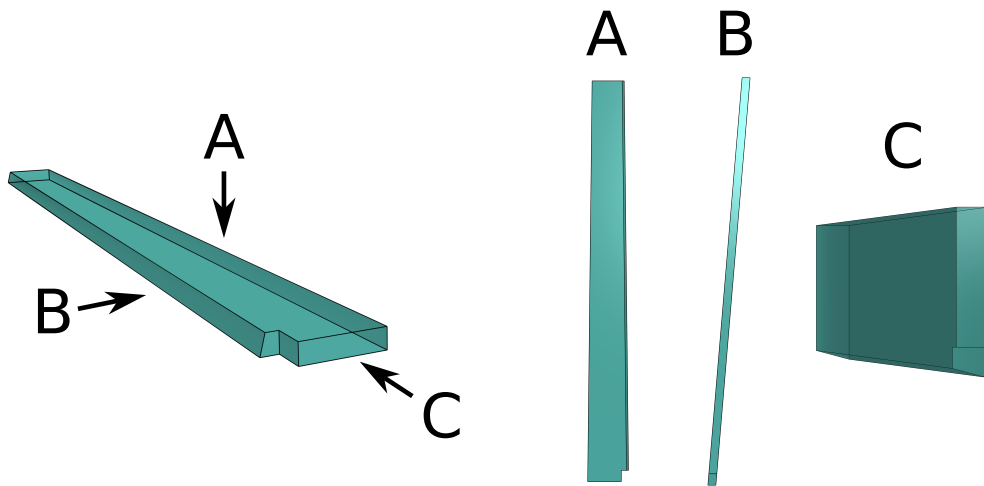

Figure A.1: CAD model of the scintillator shape, broken down into the top view (A), side view (B) and front view (C). The projection diagrams are to scale individually, but not among one another.

The main example of this is the 15 degree angle of one of the sides of the scintillator, which allows it to "mesh" with the adjacent scintillator to produce the hermetic coverage required.

A.2   Mylar wrapping

On of the more important and time-consuming parts of the detector construction is the wrapping of the scintillators in Mylar. The main goals of a good wrapping procedure are full coverage with a single layer of Mylar (as much light as possible must be contained by the wrapping), tightness (the wrapped scintillator must fit into its slot in the support structure) and speed (this process must be repeated 24 times). The solution used for this was to create a single wrapping template, whose shape is specifically designed to wrap around the given shape of the scintillators with minimal effort. This is shown in Figure A.2.
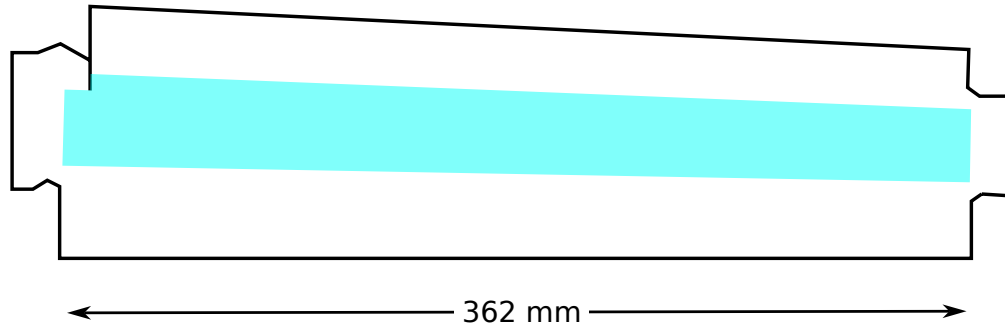

Figure A.2: Diagram of the wrapping template used for the Mylar wrapping process. The diagram is to scale, with the blue shape representing the placement of the scintillator to allow easy wrapping.

Using this template, the time taken to wrap a single scintillator can be as low as 5 minutes for a practiced wrapper.

A.3   Support structure

A specially designed 3D printed support structure (Figure A.3) is used to hold the scintillators in the final barrel shape. This design makes use of plastic rods connecting the two ends of the barrel, which allows it to be tightened to hold the scintillators securely in place (or loosened to fit the scintillators in). Furthermore, there are threaded holes placed such that the SiPM boards can be mounted on the support structure close to the SiPM end of the scintillator, thus reducing the need for lengthy cables — a rather important fact given that there are 24 of them, which could very quickly become messy. Finally, there is also space for cushioned screws, which allow the SiPMs to be pressed against the face of the scintillators, locking all the components in place and ensuring a robust overall detector.
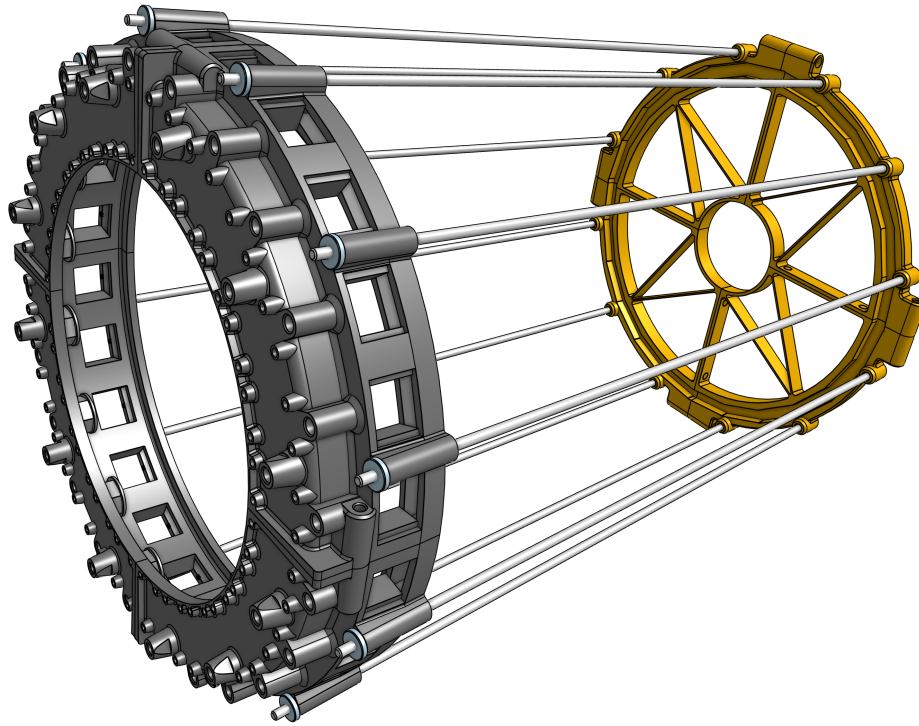
Figure A.3: CAD model of the support structure designed to hold the scintillators in place. Not shown on this model are the scintillators, SiPMs (and SiPM boards) and the external structure connecting the detector to the outside of the Crystal Ball.